PROCEEDINGS OF THE ROYAL SOCIETY A

rspa.royalsocietypublishing.org

Research

Article submitted to journal

Subject Areas:
mechanics

Keywords:
lasso, Flat Loop, whirling, bifurcation, friction, trick roping

Author for correspondence:
Pierre-Thomas Brun
e-mail: pierre-thomas.brun@eplf.ch

An introduction to the mechanics of the lasso

P.-T. Brun[1,2,3], N. Ribe[2] & B. Audoly[3]

[1]Laboratory of Fluid Dynamics and Instabilities, EPFL, 1015 Lausanne, Switzerland
[2]Laboratoire FAST, Université Paris-Sud and CNRS, Bâtiment 502, Campus Universitaire, 91405 Orsay, France
[3]Sorbonne Universités, UPMC Univ Paris 06, CNRS, UMR 7190 Institut Jean Le Rond d'Alembert, F-75005 Paris, France

Trick roping evolved from humble origins as a cattle-catching tool into a sport that delights audiences the world over with its complex patterns or 'tricks'. Its fundamental tool is the lasso, formed by passing one end of a rope through a small loop (the honda) at the other end. Here we study the mechanics of the simplest rope trick, the *Flat Loop*, in which the rope is driven by the steady circular motion of the roper's hand in a horizontal plane. We first consider the case of a fixed (non-sliding) honda. Noting that the rope's shape is steady in the reference frame rotating with the hand, we analyze a string model in which line tension is balanced by the centrifugal force and the rope's weight. We use numerical continuation to classify the steadily rotating solutions in a bifurcation diagram, and analyze their stability. In addition to *Flat Loops*, we find planar 'coat-hanger' solutions, and whirling modes in which the loop collapses onto itself. Next, we treat the more general case of a honda that can slide due to a finite coefficient of friction of the rope on itself. Using matched asymptotic expansions, we resolve the shape of the rope in the boundary layer near the honda where the rope's bending stiffness cannot be neglected. We use this solution to derive a macroscopic criterion for the sliding of the honda in terms of the microscopic Coulomb static friction criterion. Our predictions agree well with rapid-camera observations of a professional trick roper and with laboratory experiments using a 'robo-cowboy'.

Royal Society Publishing
Informing the science of the future

1. Introduction

Trick roping, originally used by Mexican *vaqueros* and American cowboys to catch cattle, has evolved into a hybrid of sport and art that involves performing various figures or *tricks* with a lasso. These range from the simplest *Flat Loop* trick through moderately difficult ones like the *Wedding Ring* and the *Merry-go-Rounds* to complicated tricks like the *Texas Skip*, in which the roper jumps back and forth through a rapidly spinning vertical loop (Fig. 1). To our knowledge, however, the physics underlying these tricks has not yet been explored in a quantitative way. Accordingly, our purpose here is to formulate and study a 'slender rope' dynamical model for the lasso that includes all the essential forces involved, thereby revealing the mathematical scaffolding that underpins trick roping.

From a mechanical point of view, a lasso is a slender elastic rod that moves and deforms subject to complex driving-, boundary-, and self-contact conditions. Bodies in this class are common in nature, industry and sport and have consequently been extensively studied. In biology, bacteria and other microscopic organisms move by waving one or more slender elastic flagellae [1]. A major industrial application is yarn manufacturing [2], where a variety of whirling modes are observed, including 'balloons' that are stationary in a co-rotating reference frame [3–6]. Finally, slender elastic rods are common in the domain of sport, from childrens' rope jumping [7] to the coiling of a mountaineer's rope played out onto the ground [8,9].

The most systematic treatment of trick roping to date is the book by Bunks [10], which describes a variety of tricks and the techniques required to master them, and gives simplified discussions of the physics involved in each. Among the most common tricks are the *Merry-Go-Rounds*, the *Wedding Ring*, *Spoke Jumping* and the *Texas Skip*. As illustrated in Figure 1, they differ in the relative position, size and orientation of the lasso and the roper. A prerequisite to master

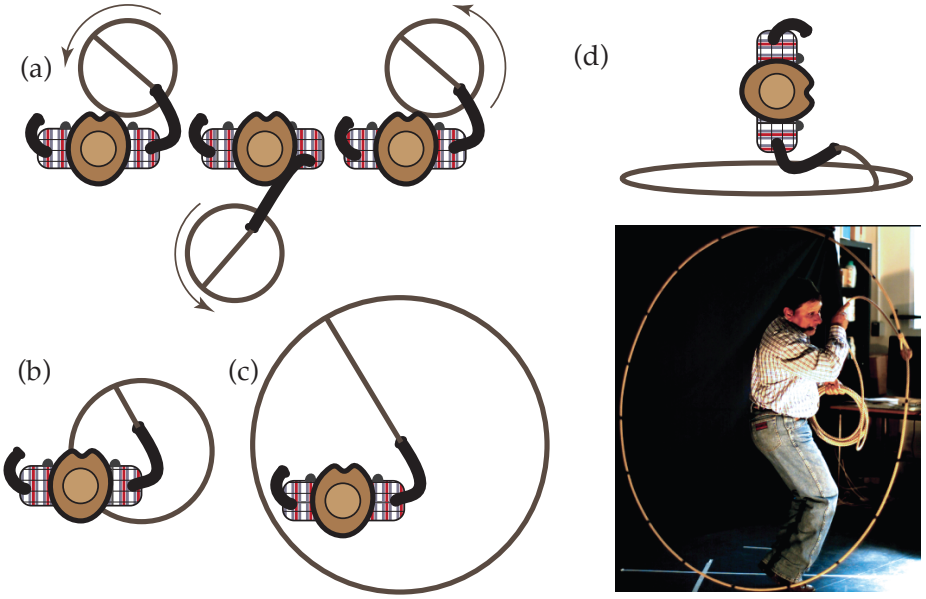

Figure 1. Four classical rope tricks: (a) *Merry-Go-Rounds*, (b) *Spoke Jumping* and (c) the *Wedding Ring*. They are all based on a flat loop of variable size and position relative to the cowboy. More complex tricks such as the *Texas Skip* (d) involve a vertical loop.

these refined tricks is thus to control the size and position of the lasso's loop. Note that all these

tricks are essentially time-dependent, as there exists no reference frame in which the motion of the lasso is stationary. This makes them difficult to master for the cowboy, and difficult to model for the physicist.

To avoid the complication of time-dependence, we focus here on the simplest of all rope tricks, the so-called *Flat Loop* (Fig. 2). In this trick, the motion of the lasso is forced by a uniform circular motion of the cowboy's hand in a horizontal plane. The cowboy's arm is extended sufficiently far from his body to avoid collisions with the rope. To avoid accumulating twist in the rope, the cowboy constantly rolls the rope between his thumb and forefinger while spinning it. The configuration of the rope is stationary in a reference frame that rotates with the hand. The portion of the rope from the hand to the honda is called the *spoke*, and the rest of the rope is called the *loop* (Fig. 2a).

2. Methods

We used three complementary approaches in our study of the mechanics of the lasso:

(a) Field observation

The first author (Brun) spent considerable time mastering the flat-loop trick and found that one of the keys to this trick is a careful initial adjustment of the relative lengths of the spoke and the loop prior to spinning, as reported by Bunks [10]. The experience gained in training by hand proved very useful in setting up the laboratory experiment described below. To complement our limited expertise, we also obtained the aid of Jesus Garcilazo (JG), a professional trick roper who works at Disneyland Paris in Marne-la-Vallée (France). During a visit to our laboratory at UPMC, he performed a variety of rope tricks that we filmed using two synchronized high-speed video cameras. Figs. 1d and 2a show JG performing the *Texas Skip* and the *Flat Loop* trick, respectively.

(b) Experiments

An experimental set-up, 'robo-cowboy', was designed to reproduce the spinning of a lasso by a cowboy, see Figure 2b. It is composed of an electric stepper motor, an arm attached to the motor's rotating axis, and a mechanical hand fixed to the arm at an adjustable distance R from the motor axis (inset in Figure 2b). The artificial hand comprises a wrist (W) that pivots freely in a vertical plane and artificial fingers (F) in the form of a cylindrical housing that is free to rotate about its axis, preventing the accumulation of twist in the rope. The angular speed of the motor may be varied continuously in the range $8.63\,\mathrm{rad\,s^{-1}} \leqslant \Omega \leqslant 20.42\,\mathrm{rad\,s^{-1}}$. We used two kinds of ropes in the experiments: either a ball chain which has negligible resistance to bending, or a cotton rope. In some experiments, the honda was a slipknot that slides along the rope with significant solid friction; in others, the sliding of the honda was prevented using adhesive tape.

(c) A rod model

Our third approach is to obtain solutions of the equations governing the dynamics of a steadily rotating lasso. We introduce a generic set of equations for an elastic rope, which we will then solve in various limits: zero or small non-zero bending rigidity, and an infinite or finite friction coefficient. Thanks to the free rotation of the rope's upper end, the twisting moment is zero everywhere and can be ignored. The steadily rotating shapes of the lasso are then governed by a balance of four forces: the rope's weight, the centrifugal force, the tensile axial stress, and the force that resists bending of the rope. In the reference frame rotating with the lasso at an angular

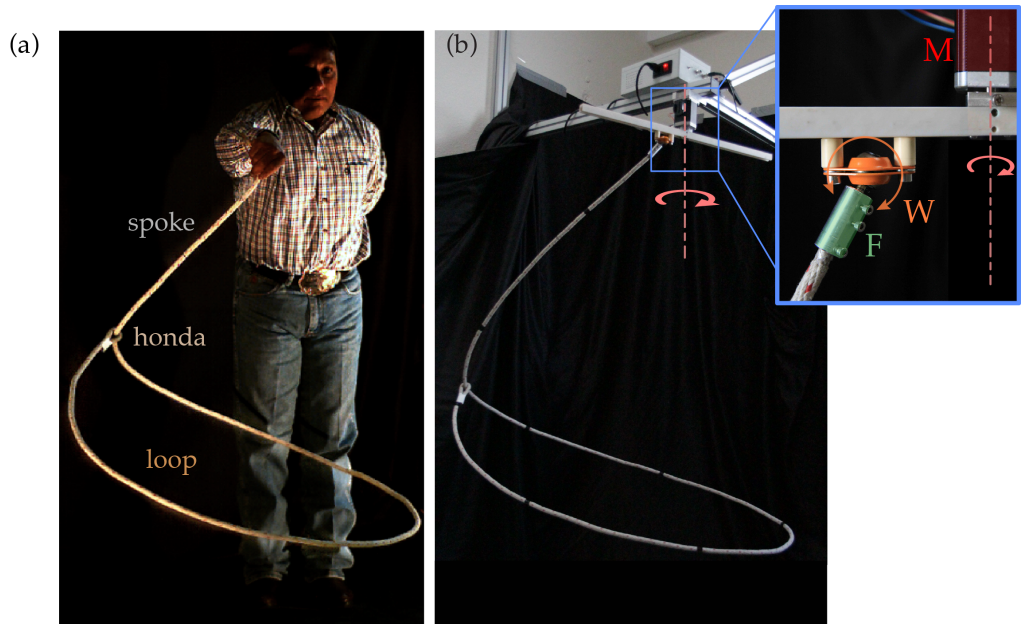

Figure 2. (a) A trick roping expert (Jesus Garcilazo) performing the *Flat Loop* trick. The lasso has a (total) curvilinear length L, and comprises a spoke of length L_s and a loop of length $L_l = L - L_s$, connected by a slipknot (the honda). (b) The experimental setup ('robo-cowboy'). The upper end of the rope is fixed in a cylindrical metal housing (F) that is free to rotate about its axis, and which is analogous to the trick roper's fingers. The upper end of the housing is in turn attached to a pivot (W) that is analogous to the roper's wrist. Finally, the pivot is attached to a bar that is rotated in a horizontal plane by a motor M.

velocity Ω, the equations are:

$$\boldsymbol{n}' + \lambda\,\boldsymbol{g} = \lambda\,\Omega^2\,\boldsymbol{e}_z \times (\boldsymbol{e}_z \times \boldsymbol{x}), \tag{2.1a}$$

$$\boldsymbol{m}' + \boldsymbol{t} \times \boldsymbol{n} = \boldsymbol{0}, \tag{2.1b}$$

$$\boldsymbol{m} = B\,\boldsymbol{t} \times \boldsymbol{t}', \tag{2.1c}$$

$$|\boldsymbol{x}'| = 1. \tag{2.1d}$$

In (2.1), λ is the mass per unit length of the rope, $\boldsymbol{g} = -g\,\boldsymbol{e}_z$ is the gravitational acceleration, $\boldsymbol{e}_z$ is the unit vector along the vertical axis, $\boldsymbol{x}(s)$ is the center-line of the rope as a function of the arclength s, $\boldsymbol{t}(s)$ is the unit vector tangent to the axis, $\boldsymbol{n}(s)$ is the internal force resultant, $\boldsymbol{m}(s)$ is the bending moment, B is the bending stiffness, and primes indicate differentiation with respect to s. Eqns. (2.1*a*) and (2.1*b*) express the balance of forces and moments, respectively, acting on an element of the rope. Eqn. (2.1*c*) is the constitutive relation for the bending moment. Finally, eqn. (2.1*d*) is the condition of inextensibility of the rope's axis. Altogether, Eqns. (2.1) are the equations for a rod having zero twisting rigidity, also know as an *elastic curve*.

The lasso problem can be expressed as two coupled problems for the spoke ($0 \leqslant s \leqslant L_s^-$) and for the loop ($L_s^+ \leqslant s \leqslant L$), which are denoted by ($\mathcal{S}$) and ($\mathcal{L}$), respectively (Figure 3). The set of equations (2.1) is valid in both domains ($\mathcal{S}$) and ($\mathcal{L}$). The boundary conditions at the two ends of the rope are

$$\boldsymbol{x}(0) = R\,\boldsymbol{e}_x, \tag{2.2a}$$

$$\boldsymbol{m}(0) = \boldsymbol{0}, \tag{2.2b}$$

$$\boldsymbol{m}(L) = \boldsymbol{0}. \tag{2.2c}$$

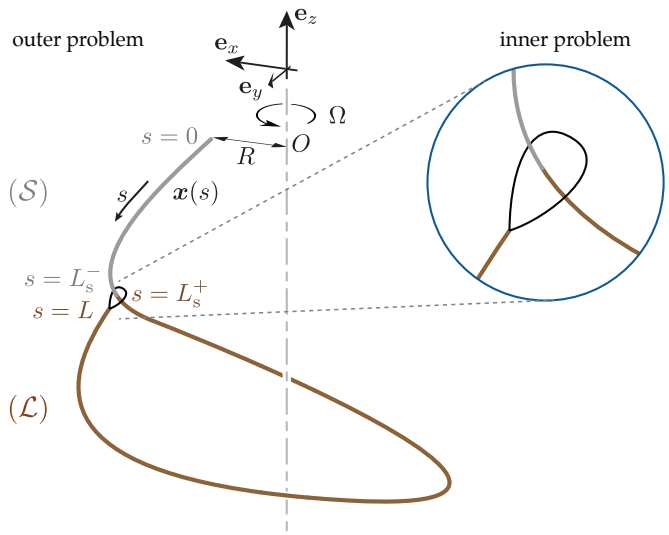

Figure 3. The Flat Loop trick is described mathematically as static solutions in a rotating frame of an inextensible string or elastic rod held at a distance R from the axis.

The matching conditions at the honda $s = L_s$ are

$$\boldsymbol{x}(L_s^-) = \boldsymbol{x}(L_s^+) = \boldsymbol{x}(L), \tag{2.3a}$$

$$\boldsymbol{x}'(L_s^-) = \boldsymbol{x}'(L_s^+), \tag{2.3b}$$

$$-\boldsymbol{n}(L_s^-) + \boldsymbol{n}(L_s^+) - \boldsymbol{n}(L) = \mathbf{0}, \tag{2.3c}$$

$$\boldsymbol{m}(L_s^-) = \boldsymbol{m}(L_s^+). \tag{2.3d}$$

Equation (2.3*a*) ensures that the position $\boldsymbol{x}$ of the rope at the end of the spoke ($s = L_s^-$) matches those at both the beginning ($s = L_s^+$) and the end ($s = L$) of the loop. Equation (2.3*b*) applies in the case where the bending stiffness $B \neq 0$, and imposes the continuity of the tangent across the honda. Eqn. (2.3*c*) expresses the balance of forces acting on the honda. Finally, eqn. (2.3*d*) expresses the balance of moments on a small segment surrounding the point of contact $s = L_s$ with the honda.

We shall first consider the case of a fixed (non-sliding) honda. Then, for any choice of the parameters B, Ω, R, L, L_s, λ, and g, we expect a unique solution in general, and in any case a *discrete* set of solutions. Dimensional analysis shows that the dynamics are governed by four dimensionless groups which represent respectively the dimensionless bending stiffness, hand radius, spoke length, and hand frequency:

$$\overline{B} = \frac{B}{L^3 \lambda g}, \quad \overline{R} = \frac{R}{L}, \quad \overline{L}_s = \frac{L_s}{L}, \quad \overline{\Omega} = \Omega \left(\frac{L}{g}\right)^{1/2}. \tag{2.4}$$

Note that we have hitherto neglected air drag. This can be justified by comparing the ratio of the typical drag force per unit length f_d and the typical centrifugal force per unit length f_c:

$$\frac{f_d}{f_c} = \frac{C_D \rho_{\text{air}} a V^2}{\lambda V^2 / L_s} \tag{2.5}$$

where C_D is the drag coefficient, ρ_{air} is the density of air, a is the rope radius, and $V \sim \Omega L_s$ is a typical velocity. Assuming $\rho_a \approx 1$ kg m^{-3}, $\lambda \approx 0.083$ kg m^{-1}, $a \approx 5$ mm, $L_s \approx 0.6$ m and C_D to

be of order 1, we find $f_d/f_c \approx 0.03$. This contrasts with the case of a jumprope, for which air drag cannot be neglected [7].

(d) Outline

The order of our presentation is influenced by the fact that $\overline{B}$ is a small number for a typical lasso. We measured the elasto-gravitational length $L_b = (B/(\lambda g))^{1/3}$ of our cotton rope by fitting its deflection as a function of the hanging length in a cantilever geometry, which gave $L_b \approx 11$ cm. For a lasso of length $L \approx 4$ m, $\overline{B} \equiv (L_b/L)^3 \sim 2 \times 10^{-5}$. In some experiments we used a ball chain in which the balls offer negligible resistance to bending as long as the curvature remains moderate.

Given the small value of $\overline{B}$, we start by seeking steadily rotating solutions for $\overline{B} = 0$. This is the *string problem* studied in section 3. We obtain solutions by numerical continuation, compare them to experiments, and analyze their stability. All this is done for a non-sliding honda, *i.e.* with a prescribed spoke length L_s.

In section 4, we study the influence of the small but non-zero bending rigidity $\overline{B}$, still for a non-sliding honda. The bending rigidity gives rise to a flexural layer in the vicinity of the point of contact with the honda, $s = L_s$, where the curvature is relatively large. Using the theory of boundary layers, we give a detailed account of this region. This enables us in particular to calculate the angle between the contact force acting at $s = L_s$ and the tangent $\mathbf{x}'(L_s)$.

In § 5, we analyze how the honda slides in the presence of dry friction, and show how this selects the curvilinear length of the spoke L_s. To do this, we use matched asymptotic expansions to combine the 'outer' (string) solution from § 3 with the 'inner' (rod) solution obtained in § 4 to provide a complete description of a lasso having a small bending rigidity $\overline{B} \neq 0$ and a finite friction coefficient $\mu_r < \infty$ (see Figure 3). In this framework, we can apply Coulomb's static friction criterion inside the flexural layer, and determine which shapes are stable with respect to friction. This allows us to discuss the selection of the relative curvilinear lengths of the loop and spoke, which we compare with laboratory experiments.

3. Outer solution: the string problem

In this section the bending stiffness $\overline{B}$ is set to zero, and the honda is not allowed to slide. In the analysis this is achieved by fixing the spoke length L_s; in the experiments, by fixing the loop to the spoke using a piece of adhesive tape.

(a) The string model

Consistent with our choice of the dimensionless parameters, we rescaled lengths using L, times using $\sqrt{L/g}$, and forces using the total weight λLg. A bar is used to denote dimensionless quantities, such as the arclength $\overline{s} = s/L$, the position $\overline{\boldsymbol{x}} = \boldsymbol{x}/L$, the internal force $\overline{\boldsymbol{n}} = \boldsymbol{n}/(\lambda Lg)$, etc.

The set of equations (2.1) are singular in the limit $\overline{B} = 0$, and only a subset of the boundary conditions (2.3) can be enforced. In particular, the conditions (2.3*c*) and (2.3*d*) on the moment and (2.3*a*) on the tangent must be discarded. We thus obtain the *string model*, whose governing equations

$$\overline{\boldsymbol{n}}' - \boldsymbol{e}_z = \overline{\Omega}^2\, \boldsymbol{e}_z \times (\boldsymbol{e}_z \times \overline{\boldsymbol{x}}), \tag{3.1a}$$

$$\overline{\boldsymbol{n}} = \overline{N}\, \overline{\boldsymbol{t}}, \tag{3.1b}$$

$$|\overline{\boldsymbol{x}}'| = 1, \tag{3.1c}$$

must be solved subject to the boundary and matching conditions

$$\overline{\boldsymbol{x}}(\overline{L}_s^-) = \overline{\boldsymbol{x}}(\overline{L}_s^+) = \overline{\boldsymbol{x}}(1), \tag{3.2a}$$

$$-\overline{\boldsymbol{n}}(\overline{L}_s^-) + \overline{\boldsymbol{n}}(\overline{L}_s^+) - \overline{\boldsymbol{n}}(1) = \boldsymbol{0}, \tag{3.2b}$$

$$\overline{\boldsymbol{x}}(0) = \overline{R}\,\boldsymbol{e}_x. \tag{3.2c}$$

In the above equations the unknown position $\overline{\boldsymbol{x}}$, tangent $\overline{\boldsymbol{t}}$, internal force $\overline{\boldsymbol{n}}$ and scalar tension $\overline{N}$ are all functions of the rescaled arclength $\overline{s}$, and a prime denotes a derivative with respect to $\overline{s}$. Note that the unit tangent is defined by $\overline{\boldsymbol{t}} = \overline{\boldsymbol{x}}'$.

From the original constitutive law (2.1*c*) and the balance of moments (2.1*b*), we recover the classical fact that the internal force in a string is along the tangent, hence equation (3.1*b*).

(b) 3D solutions by numerical continuation

Analytical solutions for a steadily rotating string can be found in implicit form in terms of elliptic integrals [12] but we opted for a numerical solution. The string problem stated above involves three dimensionless parameters, $(\overline{R}, \overline{L}_s, \overline{\Omega})$. We solved it for different values of these parameters using a numerical continuation method implemented in the open-source software library AUTO-07p [11]. The first step of the solution procedure is to specify simple mathematical forms for the spoke and the loop: in our case, we chose a horizontal circle for the loop and a straight line for the spoke. However, this initial state does not satisfy all the governing equations and boundary/matching conditions. We therefore introduced modified governing equations and boundary/matching conditions that are satisified by the initial configuration, and that contain several continuation parameters c_i. The parameters c_i are then gradually adjusted until the true governing equations and boundary/matching conditions are reached, at which point the initial solution has been transformed into the desired solution of the full unmodified problem. Some solutions obtained in this way are shown in Figure 4 for variable $\overline{R}$ or $\overline{L}_s$ with the other parameters held constant. All solutions we found exhibited mirror symmetry across the vertical plane (Oxz) passing though the cowboy's hand and the axis of rotation, even though our starting solution did not itself have this symmetry. We believe that no non-symmetric solutions exist for the string model, though we can offer no proof for this. Our symmetric solutions of the string problem will provide the outer solution of the matched asymptotic expansions when we analyze the case $\overline{B} \ll 1$ below.

(c) Experimental validation of the string model

To validate these solutions experimentally, we used a ball chain of length $L = 173$ cm mounted on the 'robo-cowboy'. The sliding motion of the honda was prevented using scotch tape. The curvilinear length L_s of the spoke is fixed at $L_s = 51$ cm, and the upper endpoint is held at a distance $R = 5.5$ cm from the axis. In view of the range of angular velocities allowed by our motor (§2(b)), the corresponding dimensionless parameters are

$$\overline{R} = 0.032, \qquad \overline{L}_s = 0.29, \qquad 3.5 \le \overline{\Omega} \le 8.5 \tag{3.3}$$

A typical experimental sequence is shown in Figure 5a. The experimental shapes are qualitatively similar to the one obtained by Jesus Garcilazo (Figure 2). A superposition of 8 experiments performed at angular velocities in the range $3.5 < \overline{\Omega} < 8.5$ is shown in Figure 5b. A good qualitative agreement is obtained with the numerically calculated equilibrium shapes. A quantitative comparison can be made using the position of the 'tip' of the loop $(\overline{x}_t, \overline{z}_t) = (\overline{x}(\overline{L}_t), \overline{z}(\overline{L}_t))$, where $\overline{L}_t = \frac{1}{2}(1 + \overline{L}_s)$ is the arc-length coordinate $\overline{s}$ at the midpoint of the loop. The agreement in Figure 5c is excellent and involves no adjustable parameter.

The dependence of the shape of the lasso on the angular velocity $\overline{\Omega}$ can be interpreted as follows. For any angular velocity, the loop is almost planar and the plane containing the loop becomes more nearly horizontal as the angular velocity is increased: large centrifugal forces tend

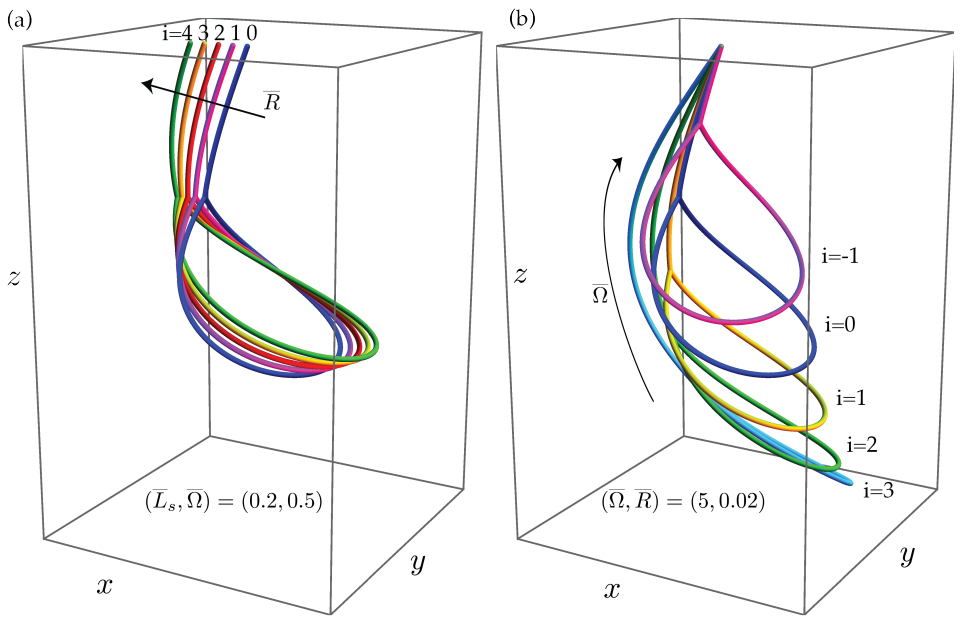

Figure 4. Solutions of the string model (3.1–3.2) for a non-sliding lasso: (a) $(\overline{L}_s, \overline{\Omega}) = (0.2, 0.5)$ and $\overline{R} = 0.02\,(i+1)$ where i is the index labelling each configuration, (b) $\overline{L}_s = 0.1\,(i+2)$ and $(\overline{\Omega}, \overline{R}) = (5, 0.02)$. The two configurations corresponding to $i = 0$ are identical.

to bring the tangents into the horizontal plane, and as a result the loop moves upwards and the spoke folds onto itself. Numerical simulations show that in the limiting case $\overline{\Omega} \to \infty$ (large angular velocity, or zero gravity), the lasso becomes planar and the spoke becomes folded at a point where the tension vanishes. Note that fold points are allowed in the string model ($\overline{B} = 0$), but are forbidden in the rope model because the bending energy penalizes curvature.

From the side, the shape of the lasso looks like the second whirling mode of a hanging chain [5]. Compared to a whirling chain, however, a loop is present, which opens up spontaneously into a roughly circular shape. In Appendix A, we carry out a detailed bifurcation analysis for the limit $R = 0$, which shows that the typical shape of the lasso in the *Flat Loop* trick arises from a combination of two bifurcations. The trivial configuration of the lasso hanging vertically with a closed loop becomes unstable beyond some critical angular velocity. Two instabilities are possible: one that opens up the loop in a vertical plane, resulting in what we call 'coat-hanger' shapes, and the other one that bends the spoke in a perpendicular vertical plane, similar to what happens when a rigid circle is attached to a spinning string [13]. Depending on the values of the parameter $\overline{L}_s$, these instabilities can take place in any order. When $R = 0$ the *Flat Loop* is obtained by combining these two bifurcations. We refer the reader to the Appendix A for details. Note that when $R \neq 0$, the bifurcation from the unbuckled configuration to whirling states disappears (imperfect bifurcation).

(d) Stability analysis of the outer solution

We also performed a stability analysis of our steadily rotating solutions using the dynamical equations governing the unsteady motion of a string. These equations, as well as the details of the stability analysis, are reported in Appendix B. The results are presented in the rest of this section, where the (complex) growth rate of the different modes is denoted by $\overline{\sigma}$.

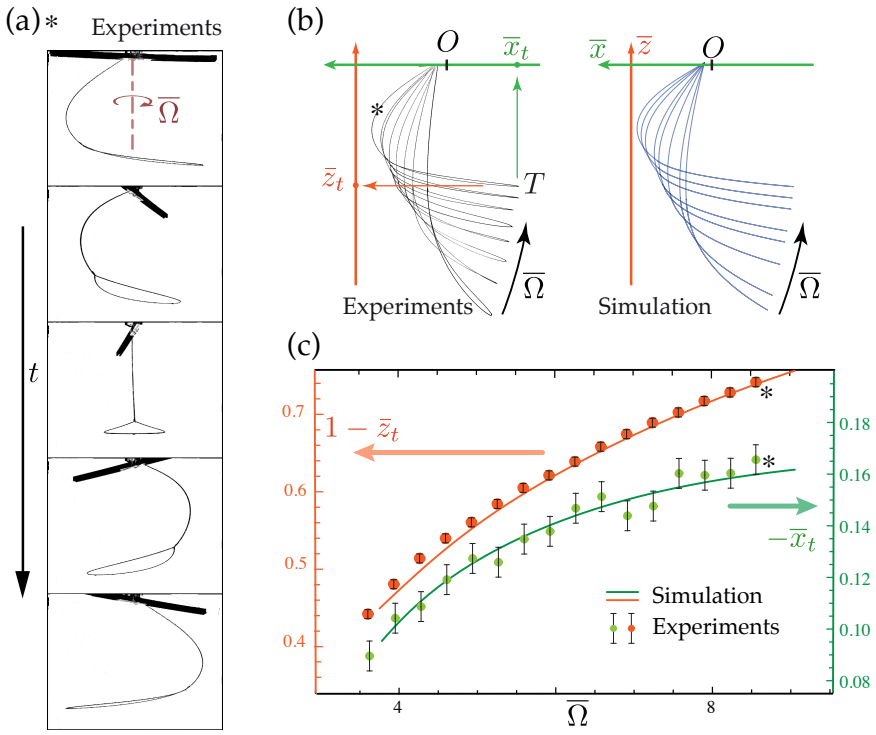

Figure 5. Experiments using a ball chain driven by our 'robo-cowboy', corresponding to the parameters listed in equation (3.3). (a) Time sequence of a full period of rotation, for $\overline{\Omega} = 8.5$. The black segment visible on top of the frames is the rotating arm of the motor. (b) Superimposed side views of experimental and numerical configurations for $\overline{R} = 0.032$, $\overline{L}_s = 0.29$, and $3.5 \leq \overline{\Omega}_s \leq 8.5$ (c) Comparison of experimental (dots) and numerical (solid curves) position of the tip T as a function of angular velocity. The configuration marked by a star in (b) and the datapoints marked by a star in (c) correspond to the time sequence shown in (a).

For each lasso configuration we always found a set of marginally stable ($\Re\overline{\sigma} = 0$) oscillatory modes with vibrational frequencies $\Im\overline{\sigma}$. The existence of such modes could have been anticipated since we are working with a string under tension. Within a narrow range of angular velocities, however, the vibrational modes are accompanied by weakly unstable modes (always the third one). For example, for $\overline{R} = 0.032$ and $\overline{L}_s = 0.29$, unstable modes exist only for $5.575 \leqslant \overline{\Omega} \leqslant 5.925$ (Figure 6). Note that the corresponding growth rates $\Re\overline{\sigma}$ are small: the fastest growing mode in Fig. 6 (at $\overline{\Omega} = 5.75$) has $\Re\overline{\sigma} \approx 0.02\,\overline{\Omega}$, which means that several tens of turns are required for the instability to be substantially amplified. Experimentally we did not observe any instability of the ball chain, probably because the various sources of dissipation in the experiments, including air drag and the friction at the joints connecting the balls, can restabilize the weak instability predicted using the non-dissipative string model.

The results of a more systematic investigation of the range of unstable parameters is presented in Figure 8 below. Numerically, we investigated the modes lying in the range $0 \leqslant \Im\overline{\sigma} \leqslant 7$, which typically contains the first six modes (this is what happens for $\overline{R} = 0.032$, $\overline{L}_s = 0.29$ and $\overline{\Omega} = 5$ for example).

4. Inner flexural layer near the honda

We have neglected the bending rigidity $\overline{B}$ of the lasso so far. This assumption is valid as long as the curvature of the rope's center line stays small, but breaks down when that curvature

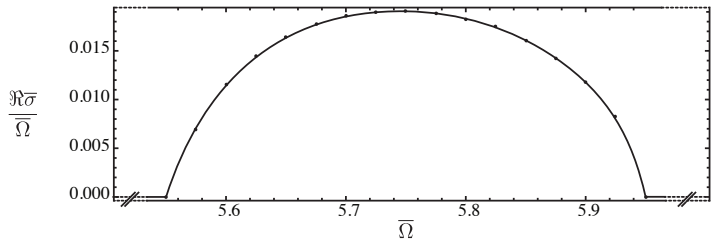

Figure 6. Largest growth rate $\Re\overline{\sigma}$ predicted by the linear stability analysis described in Appendix B, as a function of the angular velocity $\overline{\Omega}$. The same parameter values are used as in the experiments (§3(c)), namely $\overline{R}=0.032$ and $\overline{L}_s=0.29$. An instability is present in a small range of values of $\overline{\Omega}$ around $\overline{\Omega}=5.75$. There, the maximum growth rate remains small $\Re\overline{\sigma}=0.019\overline{\Omega}$. A more detailed investigation of the range of unstable parameters is presented in Figure 8.

becomes comparable to the inverse bending length $\ell_b^{-1}=(N/B)^{1/2}$, where $N\sim\lambda gL$ is the typical magnitude of the tension times cross-sectional area and B is the rope's bending stiffness. Using the string model, we found a discontinuity of the tangent at the point $\overline{s}=\overline{L}_s$ of contact with the honda, corresponding to an infinite curvature. Below, we restore the bending stress in an 'inner' layer around the honda, where it cannot be neglected, and thereby regularize the infinite curvature.

Because the tangent at the point of contact with the honda was discontinuous in the string model, Coulomb's static friction criterion for dry friction cannot be applied: it requires the direction of the tangent to be specified. One of the main benefits of the inner layer analysis below is that the direction of the tangent will be resolved, so that dry friction can be handled.

This section is concerned with analytical development: until the end of the section, we revert to physical (*i.e.* dimensional) quantities, so as to make the equations more legible.

The inner problem involves solving the equations for an elastica ($B\neq 0$), subject to appropriate matching conditions coming from the outer solution (string model, $B=0$). The inner region is the portion of the lasso within a typical distance $\sim\ell_b$ of the honda, as indicated by the shaded circle in Fig 7a. Denote the three strands of the lasso meeting at the honda by the subscripts 's' (on the spoke side), 'l' (the beginning of the loop) and 'h' (the honda, *i.e.* the end of the loop). The forces exerted by these strands on their meeting point are known from the outer solution, and are $\boldsymbol{n}_s=-\boldsymbol{n}(L_s^-)$, $\boldsymbol{n}_l=\boldsymbol{n}(L_s^+)$ and $\boldsymbol{n}_h=-\boldsymbol{n}(L)$ (see Figure 7b). Here, the signs depend on the position of each strand with respect to the honda, relative to the conventional orientation of the arc-length $\overline{s}$.

The balance of forces in equation (3.2*b*) takes the form $\boldsymbol{n}_s+\boldsymbol{n}_l+\boldsymbol{n}_h=\boldsymbol{0}$, and implies that the three strands are coplanar. Therefore, the inner problem involves solving the following equilibrium problem for two *planar* elasticas, as sketched in Figure 7b: an infinitely long *planar* elastica (made up by the strands s and l), subjected to forces $\boldsymbol{n}_l$ and $\boldsymbol{n}_s$ applied at its endpoints at infinity, is connected through a hinge to a semi-infinite planar elastica (strand h) pulled by a force $\boldsymbol{n}_h$ applied at infinity. We assume that the hinge is perfect.

We first determine the equilibrium shape of the strands s and l, using a generic analysis applicable to either one. Consider a Cartesian basis $(\boldsymbol{u},\boldsymbol{v})$, such that $\boldsymbol{v}$ is aligned with the direction of the force ($\boldsymbol{n}_s$ or $\boldsymbol{n}_l$) coming from the outer solution (Figure 7c). At distances $s\gg\ell_b$ far from the honda, the elastica is asymptotically aligned with the direction $\boldsymbol{v}$ of the applied tensile force. Let $\theta_i(s)$ be the angle between the tangent to the elastica and $\boldsymbol{v}$, where $i=s$ or l is the strand label. The tangent to the elastica, introduced earlier in equation (2.1), is $\boldsymbol{t}_i=[\sin(\theta_i),\cos(\theta_i)]$ in the Cartesian basis $(\boldsymbol{u},\boldsymbol{v})$. The equations governing the equilibrium of the elastica are derived from equations (2.1) by setting $\lambda=0$, which is valid because the effect of gravity can be neglected

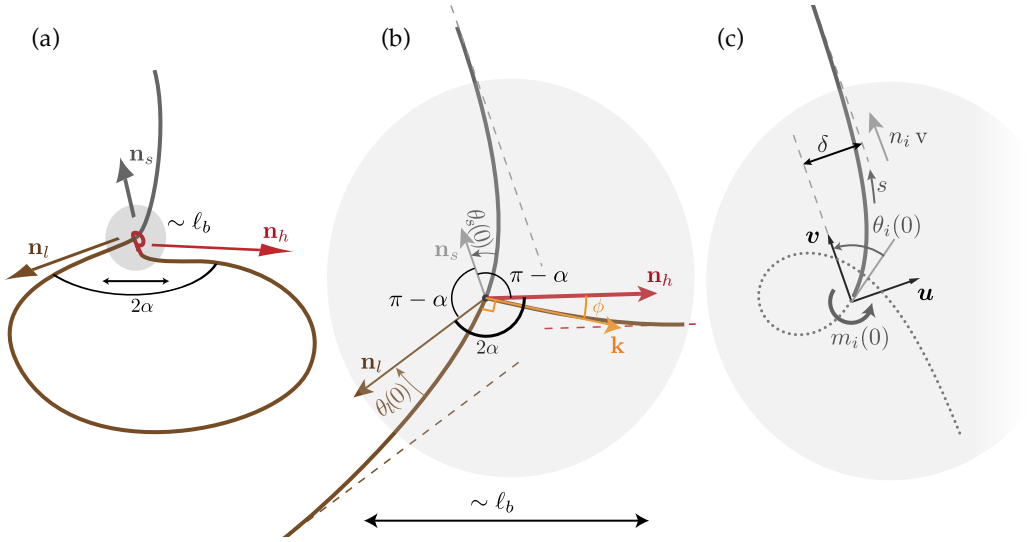

Figure 7. (a) Sketch of a the global solution: the outer (string) solution is valid far from the honda, and has to be matched with the inner solution inside the shaded disk. The equilibrium of the honda, $\boldsymbol{n}_s + \boldsymbol{n}_l + \boldsymbol{n}_h = \mathbf{0}$, implies that the inner problem is planar. By the analysis of the outer (string) problem, we know that the loop is symmetric, and define α to be half its angle at the honda. (b) The inner problem, of typical size ℓ_b. (c) Elastica solution relevant to either of the strands s or l.

within a distance $O(\ell_b)$ from the hinge. The governing equations are then

$$-B\,\theta_i' = m_i, \tag{4.1a}$$

$$m_i' + n_i\,\sin\theta_i = 0, \tag{4.1b}$$

where m_i is the bending moment in the perpendicular direction, and $n_i = |\boldsymbol{n}_i|$ is the intensity of the pulling force at infinity. Matching to the outer solution requires

$$\theta_i \to 0 \quad \text{for } s \to \infty, \tag{4.2}$$

Eliminating m_i from equations (4.1*a*) and (4.1*b*), integrating the result, and setting the constant of integration from the asymptotic condition $\theta_i \to 0$ for $s \gg \ell_b$, we obtain:

$$\frac{B}{2}\,\theta_i'^2 = n_i\,(1 - \cos\theta_i). \tag{4.3}$$

An additional integration then yields:

$$\theta_i(s) = 4\tan^{-1}\left\{\exp\left[\left(\frac{n_i}{B}\right)^{1/2}\,(s_i^0 - s)\right]\right\}, \tag{4.4}$$

where, s_i^0 is a constant of integration related to the initial slope $\theta_i(0)$. In equation (4.4), the slope θ_i decays exponentially on the lengthscale $\ell_b \equiv (B/N)^{1/2}$, as predicted above by a scaling analysis.

To match the two solutions at the honda, we observe that the symmetry of the outer solution for the loop implies $|\boldsymbol{n}_l| = |\boldsymbol{n}_h|$. The spoke force $\boldsymbol{n}_s = -(\boldsymbol{n}_l + \boldsymbol{n}_h)$ therefore bisects the angular sector spanned by $\boldsymbol{n}_l$ and $\boldsymbol{n}_h$, as shown in Figure 7b. Denoting by 2α the opening angle of the loop at the honda, as predicted by the string model, we see that both the angle between $\boldsymbol{n}_s$ and $\boldsymbol{n}_l$ and that between $\boldsymbol{n}_s$ and $\boldsymbol{n}_h$ are $(\pi - \alpha)$ (Figure 7b). In addition, $|\boldsymbol{n}_l| = |\boldsymbol{n}_h|$ implies:

$$|\boldsymbol{n}_s| = 2\,|\boldsymbol{n}_l|\,\cos\alpha \tag{4.5}$$

by simple trigonometry.

The honda applies a point force at the boundary $s = L_s$ between the spoke and the loop, where both the tangents and the bending moment are continuous. The continuity of the tangents requires $\theta_s(0) + (\pi - \alpha) - \theta_l(0) = \pi$, or

$$\theta_s(0) = \alpha + \theta_l(0). \tag{4.6}$$

The continuity of the bending moments $m_i = -B\,\theta_i'$ implies, by equation (4.3),

$$n_l\,\big(1 - \cos\theta_l(0)\big) = n_s\,\big(1 - \cos(\alpha + \theta_l(0))\big) \tag{4.7}$$

Inserting (4.5) into (4.7) and rearranging, we obtain:

$$\theta_l(0) = \pi - 2\,\alpha + \cos^{-1}(1 - 2\,\cos\alpha). \tag{4.8}$$

We have therefore derived a complete solution of the inner problem in terms of the angle α set by the outer problem.

The last step is to calculate the Coulomb angle ϕ, defined as the angle between the direction of the force $\boldsymbol{n}_h$ applied by the honda and the normal $\boldsymbol{k}$ to the elastica at the point of contact $s = L_s$, as sketched in Figure 7b. From the figure, we have $\phi + \pi - \alpha = \pi/2 + \theta_s(0)$, which yields:

$$\sin\phi = \sin\left(\alpha + \theta_s(0) - \frac{\pi}{2}\right) = 1 - 2\,\cos\alpha, \tag{4.9}$$

after elimination of $\theta_s(0)$ and $\theta_l(0)$ using (4.6) and (4.8). The tangent of the Coulomb angle can therefore be expressed as:

$$\tan\phi = f(\cos\alpha) \qquad \text{where } f(u) = \frac{\frac{1}{2} - u}{\sqrt{u\,(1-u)}}. \tag{4.10}$$

To sum up: at this point, we have derived (*i*) the outer solution by solving a string problem (§3), and (*ii*) the inner solution by solving the flexural layer (§4). The latter allows us to calculate the Coulomb angle in terms of the former. We can therefore proceed to re-examine the solutions of the string problem, now addressing the possibility of frictional slip at the honda.

5. Combining inner and outer solutions and comparing with experiments

To combine the inner and outer solutions, we use equation (4.10) connecting the macroscopic angle α of the string model to the microscopic Coulomb angle ϕ. It allows Coulomb's static friction criterion $|\tan\phi| < \mu_r$ to be expressed by

$$\begin{cases} |f(\cos\alpha)| < \mu_r & \text{(stick)} \\ |f(\cos\alpha)| = \mu_r & \text{(slip)} \end{cases} \tag{5.1}$$

where μ_r is the friction coefficient of the rope on itself. Using this equation, we can determine the state of the honda as a function of the macroscopic angle α. In particular, the frictionless case $\mu_r = 0$ corresponds to $f = 0$, hence $\cos\alpha = \frac{1}{2}$:

$$\alpha = \frac{\pi}{3} \quad \text{(frictionless case, } \mu_r = 0). \tag{5.2}$$

We now use this effective, 'macroscopic' criterion of friction to revisit the solutions of the string models that we derived in Section 3 under the assumption of a fixed honda. For every value of the triple $(\overline{R}, \overline{L}_s, \overline{\Omega})$ we evaluate the angle $\alpha(\overline{R}, \overline{L}_s, \overline{\Omega})$ made by the loop at the honda, using the numerical solution of the string problem. Then, we define μ_r^* by

$$\mu_r^*(\overline{R}, \overline{L}_s, \overline{\Omega}) = f\Big(\cos\big(\alpha(\overline{R}, \overline{L}_s, \overline{\Omega})\big)\Big). \tag{5.3}$$

By equation (5.1), the state of the solution described by the set of parameters $(\overline{R}, \overline{L}_s, \overline{\Omega})$ can be predicted by comparing the true friction coefficient of the rope μ_r to the limit value μ_r^* predicted

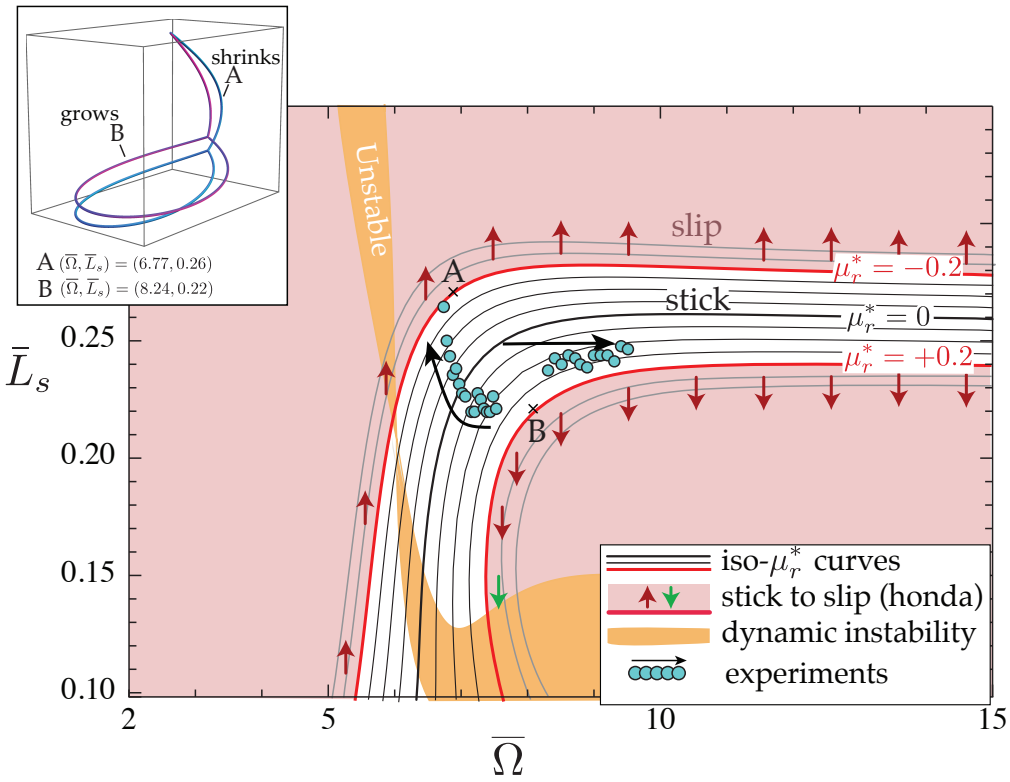

Figure 8. Diagram of stability of the lasso in the $(\overline{\Omega}, \overline{L}_s)$ plane, for $\overline{R} = 0.032$. The parallel black and red curves show the isovalues of μ_r^* predicted by the matched asymptotic expansions: the central thick black curve corresponds to frictionless solutions ($\mu_r^* = 0$), and the red curves show the onset of sliding ($\mu_r^* = \pm\mu_r$) at the honda for a Coulomb coefficient $\mu_r = 0.2$. Two particular configurations on these curves are shown in insets A and B. Near the red curves, the red (unstable) and green (stable) arrows represent the lasso behavior after the onset of sliding at the honda, as discussed in the main text. The orange region marks the linearly unstable domain based on the stability analysis of Appendix B. Green dots correspond to two experimental datasets ($R = 12.7$ cm, $L = 396$ cm, corresponding to the same $\overline{R} = 0.032$), obtained with a cotton lasso for slowly increasing and decreasing angular frequencies; the arrows indicate the order in which these points were measured.

by the theory:

$$\begin{cases} |\mu_r^*(\overline{R}, \overline{L}_s, \overline{\Omega})| < \mu_r & \text{(stick)} \\ |\mu_r^*(\overline{R}, \overline{L}_s, \overline{\Omega})| = \mu_r & \text{(slip)} \end{cases} \tag{5.4}$$

In other words, $|\mu_r^*|$ is the *minimum* value of the friction coefficient μ_r required for the honda to be blocked.

The isoclines of μ_r^* are plotted as curves in the $(\overline{\Omega}, \overline{L}_s)$ plane in Figure 8, for a fixed value of the offset $\overline{R} = 0.032$ matching that from our experiments. In the parameter space reported in Figure 8, which corresponds to the imperfect case ($\overline{R} \neq 0$), we were always able to find *Flat loop* solutions. In view of equation (5.4), the steady solutions that can be observed for a given value μ_r of the rope friction coefficient are those enclosed by the curves $\mu_r^* = -\mu_r$ and $\mu_r^* = +\mu_r$ in the diagram (thick red curve in Figure 8). The central dotted curve is the locus of equilibrium solutions that can hold without any friction ($\alpha = \pi/3$, $\mu_r^* = 0$). Above the upper curve $\mu_r^* = -\mu_r$ the honda starts to slide in the direction that makes the loop shrink: $f < 0$ implies $\alpha < \pi/3$, as for the configuration A in

Figure 8, and $\overline{L}_s$ increases, as indicated by the vertical arrows. Conversely, below the lower curve $\mu_r^* = +\mu_r$, the honda slides in the direction that makes the loop grow: $f > 0$ implies $\alpha > \pi/3$, as in the configuration B in Figure 8, and $\overline{L}_s$ decreases, as indicated by the vertical arrows. In the experiment, the angular velocity $\overline{\Omega}$ is controlled. Except in a very small region of the boundary (green vertical arrow, near $\overline{\Omega} = 7.5$), the sliding motion sketched by the red vertical arrows pushes the system even further from the region of frictional blockage: therefore, we expect that the system becomes unstable whenever the honda starts to slip.

Superimposed on the diagram are the results of the stability analysis carried out in Appendix B. The orange area denotes unstable configurations. Everywhere outside this orange area Figure 8, there exist stable *Flat Loop* solutions. The stability analysis assumed that the honda cannot slide. This assumption is justified when the coefficient of static friction is non-zero: as long as the base solution lies in the interior of the region of frictional blockage ($|\mu_r^*| < \mu_r$), no infinitesimal perturbation can violate Coulomb's static friction criterion, and the stability analysis must indeed assume that the honda remains in the blocked state.

To summarize, the analysis predicts that steadily rotating solutions can be observed in the white central band in the diagram bounded by the two red curves $\mu_r^* = \pm\mu_r$ (where the honda is in the blocked state), excluding the orange tongues (where a dynamical instability is expected to take place).

To compare this phase diagram to experiments done using a real lasso, we started by measuring the value of the friction coefficient μ_r of a cotton lasso rope on itself. We used a simple 'cable car' experiment set up as follows. A weight was suspended to a short piece of rope terminated by a honda which could slide onto another piece of rope clamped at its endpoints and subjected to tension. The tension was large enough that it stays almost straight in the presence of the weight. We varied the slope of the second rope with respect to the horizontal, and measured the slope angle at the onset of sliding. The arc-tangent of this angle yields the value of μ_r, which we found to be $\mu_r \approx 0.2$ for our rope.

Next, we produced experimental datapoints in the phase diagram in Figure 8 as follows. We used the same cotton lasso as in the calibration experiments ($\mu_r = 0.2$). Its honda is a standard slipknot and can slide with friction. The lasso was fixed onto our 'robo-cowboy' ($R = 12.7$ cm and $L = 396$ cm). Once the lasso has been attached to the mechanical hand, the motor was turned on at an initial angular frequency, and the operator intervened by hand to guide the rotating system into a *Flat Loop* configuration. The frequency was then gradually decreased from $\overline{\Omega_1} = 7.54$ to $\overline{\Omega_2} = 6.74$ and increased from $\overline{\Omega}_3 = 8.33$ to $\overline{\Omega}_4 = 9.53$. The spoke length $\overline{L_s}$ was measured on steadily rotating configurations for a series of values of $\overline{\Omega}$. The initial values $\overline{L_s}(\overline{\Omega_1})$ and $\overline{L_s}(\overline{\Omega_3})$ depend on the way the operator initiates the *Flat Loop* , hence the gap between the two sets of data. The experimental datapoints all fall inside the white region of the diagram: the experiments are fully consistent with the analysis. The dataset corresponding to increasing $\overline{\Omega}$ is distributed along a horizontal line in the diagram: $\overline{L}_s$ remains constant, consistent with the fact that neither slip at the honda nor a dynamical instability are predicted by the theory. At the maximum value of $\overline{\Omega}$ reported in the diagram, the lasso started to collide with the walls of the experimental room (for larger $\overline{\Omega}$ its shape is both flatter and wider), and we stopped the experiments. For the other dataset, corresponding to decreasing $\overline{\Omega}$, $\overline{L}_s$ first remains constant. Then, for a reason which is unclear [1], $\overline{L}_s$ starts to increase quasi-statically, corresponding to a progressive shrinkage of the loop. At some even lower angular frequency $\overline{\Omega}$ corresponding to the last datapoint (close to A in the diagram), we found that the loop collapses suddenly. This collapse occurs exactly when the system encounters the boundary $\mu_r^* = \mu_r$, where the theory indeed predicts an instability (unstable stick to slip transition, as indicated by the red vertical arrow in the diagram).

[1]The points in the dataset are parallel to the boundary of the unstable region (orange in the diagram), but with some offset. One possible explanation for the variations of $\overline{L}_s$ upon decreasing $\overline{\Omega}$ is that the dynamical instability takes place slightly earlier than predicted by the theory, and causes slip at the honda, in such a way that the system moves spontaneously along the edge of the unstable region.

6. Discussion and conclusions

The phase diagram of Fig. 8 enables us to draw some practical conclusions about trick roping.

First, the typical angular velocities one can produce with one's arm ($\lesssim 120$ rpm, or $\overline{\Omega} \lesssim 7.9$) have a good overlap with the range of angular frequencies where steadily rotating solutions exist, confirming what we already know from experience: that the *Flat Loop* trick is indeed possible. But the diagram also predicts that a minimal angular frequency of $\overline{\Omega} \sim 5.5$ (corresponding to 1.4 turns per second, or 84 rpm) is required to produce flat loops. A key to success is therefore to pick a good angular velocity.

Second, the diagram shows that the relative size $\overline{L}_s$ of the loop to the total arc-length has to lie in a narrow interval. Our theory does a very good job at explaining the narrow range of values $0.20 \lesssim \overline{L}_s \lesssim 0.30$ in which we could produce *Flat Loop* configurations experimentally. Practically, this means that the loop needs to comprise initially about $\sim 75\%$ of the total rope length for the *Flat Loop* trick to succeed. This was confirmed by Jesus Garcilazo (personal communication) and by the experiment in Fig 2a, for which $L_s = 0.74L$. Beginners often tend to form smaller loops (larger $\overline{L}_s$) but such configurations are unstable as the honda slides and the loop shrinks to a point.

Third, we found that $\overline{L_s}$ becomes independent of the forcing (hand) frequency when that frequency becomes large: the lasso then only changes its shape by becoming flatter and rising close to the level of the cowboy's hand. This implies that changing the angular frequency is of little help in adjusting the loop size. A corollary is that cowboys cannot adjust the size of their lasso by slowly (quasi-statically) changing the forcing parameters. We speculate that a sudden change of the forcing parameters (radius or frequency) may be necessary for this purpose.

An unexpected conclusion of our study is that the *Flat Loop* trick has mirror symmetry across a vertical plane passing through the rotation axis and the hand. This counterintuitive conclusion implies that the hand does not 'lead' the honda, but rather remains perfectly in phase with it. By contrast, Bunks [10] asserts that the hand leads the honda by 90°, and our collaborator Jesus Garcilazo affirmed to us that it 'feels like' the hand is leading. However, numerical modeling and the rapid-camera observations provided in the supplementary material support the opposed conclusion of perfect mirror symmetry.

This first venture into the mechanics of the lasso focused on the *Flat Loop* trick, which is the simplest shape and the only one that is stationary in a co-rotating reference frame. In future we plan to extend the present analysis to non-stationary situations, a category that includes the most spectacular tricks in the roper's toolkit. An interesting question for future work is to understand how ropers control their lassos based on visual and/or tactile input, a feedback that may have a strongly stabilizing effect.

Acknowledgements

This paper is dedicated to the memory of the late Vince Bruce, one of the great trick ropers of our time. We would like to thank Jesus Garcilazo for his participation and expertise, which helped us immeasurably to understand the subtleties of trick roping. We are grateful to the engineers and technichens of FAST who created 'robo-cowboy': L. Auffray (design), A. Aubertin (instrumentation), and R. Pidoux (construction). We would also like to thank Antoine Fouchier for his participation in the realization of preliminary experiments. PTB thanks François Gallaire and Cristobal Arratia for discussions on the stability analysis part of the problem. PTB was partially funded by the ERC grant SIMCOMICS 280117.

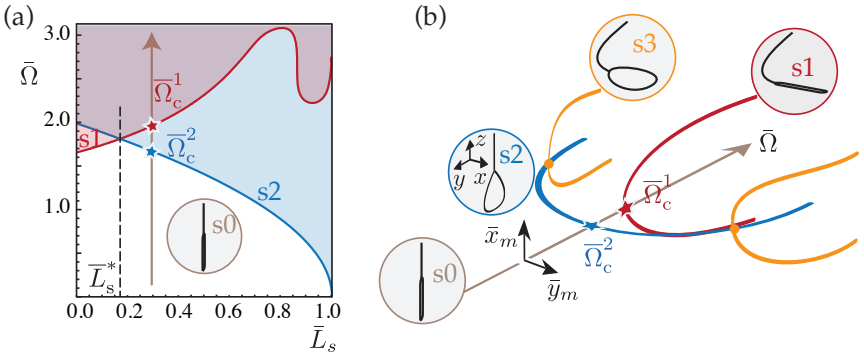

Figure 9. Bifurcation analysis of a lasso with a non-sliding honda ($\mu_r = \infty$), with the upper endpoint lying on the axis ($\overline{R} = 0$). *Flat Loops* are obtained from the unbuckled (straight, vertical) configuration s0 by a succession of two bifurcations. (a) Bifurcation analysis of the unbuckled configuration s0 showing a competition of the whirling instability (s1: loop stays closed, string becomes curved) and 'coat-hanger' instability (s2: loop opens up, spoke remains straight) : the critical rotation frequencies are plotted as a function of the spoke length $\overline{L}_s$. The coat-hanger mode occurs first when $\overline{L} > \overline{L}_s^* = .167$ (b) Bifurcation diagram as a function of the rotation frequency $\overline{\Omega}$, for $\overline{L}_s = .29$, showing the branches corresponding to the trivial solution (s0), the whirling modes (s1), the hanger mode (s2) and the *Flat Loop* mode (s3). The unbuckled solution first becomes unstable to a hanger mode (planar solution with open loop, s2); at a higher frequency, the hanger mode loses planar symmetry and goes to a lasso shape, s3, by a secondary bifurcation.

A. Appendix: bifurcation diagram for whirling solutions, coat-hangers and flat loops

We consider the string model for the lasso in equations (3.1–3.2) with a non-sliding honda ($\mu_r = \infty$), and report the existence of four types of solution in the case $\overline{L}_s = 0.29$ and $\overline{R} = 0$, *i.e.* when the upper end of the lasso coincides with the axis of rotation (Figure 9).

The first type of solution, denoted by 's0', is when the lasso is hanging along the axis $\boldsymbol{e}_z$ and its loop is closed. We will refer to this as the trivial branch of solutions.

The second family of solutions, denoted by 's1', are whirling solutions: the loop is closed but the string deviates from the axis of rotation. Mathematically, these solutions are classical whirling modes [4–6] of an inhomogeneous string having a mass per unit length λ in its upper part (in the spoke, above the honda) and $2\,\lambda$ in its lower part (in the loop, made up of two braids in contact). The length of this whirling string is $L_s + \frac{1}{2}(L - L_s)$.

The third type of solutions are 'coat-hanger' solutions, denoted by 's2'. A solution of this type is planar and stays invariant by a planar reflection with respect to the axis of rotation. Their plane rotates with an angular velocity Ω, and the loop is opened up by centrifugal forces.

Finally, the *Flat Loop* solutions, denoted by 's3' are non-planar solutions: the spoke lies in a plane that in an axis of symmetry of the loop. Solutions without this symmetry appear not to exist. These *Flat Loop* solutions have been extensively discussed in the main text.

Using numerical continuation, we studied the possible bifurcations from the trivial state 's0'. We found a competition between two possible bifurcations, one leading to whirling modes and the other one to coat-hanger solutions. The corresponding bifurcation thresholds are plotted in Figure 9a as a function of the dimensionless spoke length $\overline{L}_s$. For $\overline{L}_s$ less than a critical value $L_s^* = .167$, the whirling mode appears first; for $\overline{L}_s > \overline{L}_s^*$, the coat-hanger mode appears first.

In Figure 9b, we show the bifurcation diagram for a fixed value of $\overline{L}_s = 0.29$ (and $\overline{R} = 0$ as everywhere in this appendix). The angular velocity $\overline{\Omega}$ is used as a control parameter. To identify

the configurations, we used two order parameters,

$$\overline{x}_m = \frac{1}{\overline{L}} \max_{s\in[\overline{L}_s,\overline{L}]} x(s), \qquad \overline{y}_m = \frac{1}{\overline{L}} \max_{s\in[\overline{L}_s,\overline{L}]} y(s), \tag{A.1}$$

where the axes are oriented in such a way that the plane (Oxz) contains the spoke, and is the plane of symmetry of the loop. The trivial branch 's0' corresponds to $\overline{x}_m = \overline{y}_m = 0$, the whirling solutions 's1' to $\overline{x}_m \neq 0$ and $\overline{y}_m = 0$, the coat-hanger solutions 's2' to $\overline{x}_m = 0$ and $\overline{y}_m \neq 0$, and the *Flat Loop* solutions to both $\overline{x}_m \neq 0$ and $\overline{y}_m \neq 0$.

For the particular value of $\overline{L}_s$ shown in Figure 9a, the *Flat Loop* state 's3' is obtained by a bifurcation from the coat-hanger branch 's2', not from the whirling modes 's1'. The same holds for any value of $\overline{L}_s$. Doing the experiments by hand, we indeed found that it was virtually impossible to open the loop once trapped in a whirling state.

Based on this diagram, the *Flat Loop* solutions can be understood as resulting from a series of two bifurcations: one that opens up the loop and the other one that bends the spoke away from the axis of rotation. *Flat Loops* are a hybrid of coat-hangers and whirling solutions. Note that in the case where $R \neq 0$ the evoked bifurcations are then imperfect.

B. Appendix: Linear stability analysis of the string model

We begin with the equations of motion for the lasso based on the string model, with a non-sliding honda. These equations are then linearized to analyze the stability of steadily rotating solutions in the dynamical sense.

The base solution is of the type described in §3 — see Figure 4 in particular — and is stationary in the co-rotating frame. Let us denote by a subscript 0 this base solution, $(\overline{\boldsymbol{x}}_0(\overline{s}), \overline{\boldsymbol{n}}_0(\overline{s}))$, and the set of associated dimensionless parameters $(\overline{R}_0, \overline{L}_{s0}, \overline{\Omega}_0)$. Because the base state and the equations of motion are time-invariant, we introduce time-dependent perturbations of the form $\overline{\boldsymbol{x}}_1(\overline{s},\overline{t}) = \overline{\boldsymbol{x}}_1(\overline{s})\, e^{\overline{\sigma}\,\overline{t}}$ and $\overline{\boldsymbol{n}}_1(\overline{s},\overline{t}) = \overline{\boldsymbol{n}}_1(\overline{s})\, e^{\overline{\sigma}\,\overline{t}}$, where the dimensionless growth rate $\overline{\sigma}$ is a complex number.

We restore the complete acceleration term in equation (3.1*a*), insert the expansions $\overline{\boldsymbol{x}} = \overline{\boldsymbol{x}}_0 + \overline{\boldsymbol{x}}_1$ and $\overline{\boldsymbol{n}} = \overline{\boldsymbol{n}}_0 + \overline{\boldsymbol{n}}_1$ and linearize to obtain

$$\overline{\boldsymbol{n}}_1' = \overline{\sigma}^2\, \overline{\boldsymbol{x}}_1 + 2\overline{\sigma}\,\overline{\Omega}_0\, \boldsymbol{e}_z \times \overline{\boldsymbol{x}}_1 + \overline{\Omega}_0\, \boldsymbol{e}_z \times (\overline{\Omega}_0\, \boldsymbol{e}_z \times \overline{\boldsymbol{x}}_1). \tag{B.1a}$$

The three terms in (B.1*a*) represent the acceleration seen within the co-rotating frame, the Coriolis acceleration, and the centrifugal acceleration, respectively. Note that none of the control parameters $(\overline{R}_0, \overline{L}_{s0}, \overline{\Omega}_0)$ is perturbed.

Rewriting the constitutive law (3.1*b*) and the inextensibility condition (3.1*c*) as $\overline{\boldsymbol{x}}' = \overline{\boldsymbol{n}}/|\overline{\boldsymbol{n}}|$, we find upon linearization

$$\overline{\boldsymbol{x}}_1' = \frac{\overline{\boldsymbol{n}}}{|\overline{\boldsymbol{n}}|} - \frac{\overline{\boldsymbol{n}}_0}{|\overline{\boldsymbol{n}}_0|} = \frac{\overline{\boldsymbol{n}}_1}{|\overline{\boldsymbol{n}}_0|} - \frac{\overline{\boldsymbol{n}}_0}{|\overline{\boldsymbol{n}}_0|}\frac{\overline{\boldsymbol{n}}_0 \cdot \overline{\boldsymbol{n}}_1}{\overline{\boldsymbol{n}}_0^2}, \tag{B.1b}$$

where the right-hand side is the projection of $\overline{\boldsymbol{n}}_1$ in the direction perpendicular to $\overline{\boldsymbol{n}}_0$.

The set of equations (B.1) applies to both the linearized spoke ($\mathcal{S}$) and loop ($\mathcal{L}$) domains. The relevant boundary and continuity conditions are derived from equation (3.2) and are:

$$\overline{\boldsymbol{x}}_1(0) = \boldsymbol{0}, \tag{B.2a}$$

$$\overline{\boldsymbol{x}}_1(\overline{L}_s^+) - \overline{\boldsymbol{x}}_1(\overline{L}_s^-) = \boldsymbol{0}, \tag{B.2b}$$

$$\overline{\boldsymbol{x}}_1(1) - \overline{\boldsymbol{x}}_1(\overline{L}_s^+) = \boldsymbol{0}. \tag{B.2c}$$

where $\overline{L}_s^-$ and $\overline{L}_s^+$ refer to either side of the honda. The honda is massless: therefore, the balance of forces is

$$-\,\overline{\boldsymbol{n}}_1(\overline{L}_s^-) + \overline{\boldsymbol{n}}_1(\overline{L}_s^+) + \overline{\boldsymbol{n}}_1(1) = \boldsymbol{0}. \tag{B.2d}$$

The boundary value problem comprising equations (B.1) along with the boundary conditions (B.2) is integrated numerically using a shooting method. The missing initial

data in each domain, $\mathcal{V} = (\overline{\boldsymbol{n}}_1(0), \overline{\boldsymbol{n}}_1(\overline{L}_s^+))$, are used as shooting parameters. We denote by $\boldsymbol{M}(\overline{\sigma}, \overline{R}_0, \overline{L}_{s0}, \overline{\Omega}_0)$ the shooting matrix, such that $\boldsymbol{M}(\overline{\sigma}, \overline{R}_0, \overline{L}_{s0}, \overline{\Omega}_0) \cdot \mathcal{V} = \mathcal{R}$ yields the residue $\mathcal{R}$ for any particular value of the initial condition $\mathcal{V}$. Here, the residue is defined as the left-hand sides of equations (B.2*c*) and (B.2*d*). The matrix $\boldsymbol{M}$ is a 6×6 matrix. As usual for the shooting method, the columns of $\boldsymbol{M}$ are found by calculating the residues corresponding to the six particular initial conditions such that $\mathcal{V}$ has only zero entries, except for one entry which is set to unity.

Integrating the linearized problem six times, we can therefore calculate the matrix $\boldsymbol{M}$. The complex growth rates $\overline{\sigma}$ are then the solutions of

$$\boldsymbol{M}(\overline{\sigma}, \overline{R}_0, \overline{L}_{s0}, \overline{\Omega}_0) \cdot \mathcal{V} = \boldsymbol{0}. \tag{B.3}$$

Non-trivial solutions of equation (B.3) exist when $\det(\boldsymbol{M}(\overline{\sigma}, \overline{R}_0, \overline{L}_{s0}, \overline{\Omega}_0)) = 0$, which is an eigenvalue problem for $\overline{\sigma}$. For a given base solution labelled by $(\overline{R}_0, \overline{L}_{s0}, \overline{\Omega}_0)$, the set of complex growth rates $\overline{\sigma}$ are found by numerical root-finding. The base solution is dynamically stable if all roots $\overline{\sigma}$ have a negative real part, $\Re\overline{\sigma} \leq 0$, and dynamically unstable otherwise. Note that there are infinitely many eigenvalues and the denomination stable is relative to the number of eigenvalues investigated, generally the first six. In facts, even when checking more, we have found that only the third one was likely to become unstable.

The stability region in the diagram in Figure 8 has been obtained by meshing the region of interest, $3.0 < \overline{\Omega} < 9.0$ and $0 < \overline{L}_s < 0.35$. Each point in the mesh corresponds to a particular base solution, whose stability has been assessed using the method described above.

References

1. CW Wolgemuth, and TR Powers and RE Goldstein, 2000 Twirling and whirling: Viscous dynamics of rotating elastic filaments. *Phys. Rev. Lett.* 84(7), 1623–1626.
2. W B Fraser, 1993 On the Theory of Ring Spinning. *Phil. Trans. R. Soc A*, 342(1665):439–468.
3. Fang Zhu, Kevin Hall, and Christopher D Rahn. 1998 Steady state response and stability of ballooning strings in air. *Int. J. Non-Linear Mechanics*, 33(1):33–46.
4. G Lemon and W B Fraser, 2001 Steady-state bifurcations and dynamical stability of a heavy whirling cable acted on by aerodynamic drag. *Proc. R. Soc. A*, 457(2009):1021–1041.
5. J Coomer, M Lazarus, RW Tucker, D Kershaw, and A Tegman. 2001 A non-linear eigenvalue problem associated with inextensible whirling strings. *J. Sound Vib.*, 239(5):969–982
6. JD Clark, WB Fraser, CD Rahn, and A Rajamani. 2005 Limit–cycle oscillations of a heavy whirling cable subject to aerodynamic drag. *Proc. R. Soc. A*, 461(2055):875.
7. J. M Aristoff and H. A Stone. The aerodynamics of jumping rope. *Proc. Soc. A*, 468(2139):720–730, 2012.
8. L. Mahadevan and Joseph B. Keller. Coiling of flexible ropes. *Proc. R. Soc. A*, 452, 1996.
9. M Habibi, N Ribe, and Daniel Bonn. Coiling of Elastic Ropes. *Phys. Rev. Lett.*, 99(15):154302, October 2007.
10. C. Bunks. 1996 *A rational guide to trick roping*. See http://www.juggling.org/books/lasso/ .
11. E. J. Doedel, A. R. Champneys, T. F. Fairgrieve, Y. A. Kuznetsov, B. Sandstede, and X. J. Wang 2007 AUTO-07p: continuation and bifurcation software for ordinary differential equations. See http://indy.cs.concordia.ca/auto/ .
12. J. A. Hanna. Rotating strings. *Journal of Physics A: Mathematical and Theoretical*, 46(23):235201, 2013.
13. F Moisy. Supercritical bifurcation of a spinning hoop. *Am. J. Phys.*, 2003.